Micron 116 (2019) 54–60

Contents lists available at ScienceDirect

Micron

journal homepage: www.elsevier.com/locate/micron

Hole free phase plate tomography for materials sciences samples

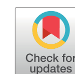

Misa Hayashida[a,*], Kai Cui[a], Amin Morteza Najarian[b], Richard McCreery[a,b], Neerushana Jehanathan[c], Chris Pawlowicz[c], Sohei Motoki[d], Masahiro Kawasaki[e,1], Yuji Konyuba[d], Marek Malac[a,f]

[a] NRC-NANO, 11421 Saskatchewan Drive, Edmonton, Alberta, T6G 2M9, Canada
[b] Department of Chemistry, University of Alberta, Edmonton, T6G 2G2, Canada
[c] TechInsights, 1891 Robertson Rd #500, Nepean, ON K2H 5B7, Canada
[d] JEOL Ltd. 3-1-2 Musashino, Akishima, Tokyo 196-8558, Japan
[e] JEOL USA Inc. 11 Dearborn Rd, Peabody, MA 01960, USA
[f] Department of Physics, University of Alberta, Edmonton, Alberta, T6G 2E1, Canada

ARTICLE INFO

Keywords:
Hole free phase plate (HFPP)
Electron tomography
Transistor imaging
Molecular electronic junction
Interface roughness
Transmission electron microscope (TEM)

ABSTRACT

We report, for the first time, the three dimensional reconstruction (3D) of a transistor from a microprocessor chip and roughness of molecular electronic junction obtained by electron tomography with Hole Free Phase Plate (HFPP) imaging. The HFPP appears to enhance contrast between inorganic materials and also increase the visibility of interfaces between different materials. We demonstrate that the degree of enhancement varies depending on material and thickness of the samples using experimental and simulation data.

1. Introduction

Differentiation of the various layers in a semiconductor device is becoming increasingly more difficult as device dimensions decrease. The typical layer thickness in a 22 nm node devices is in the order of a few nanometers, i.e. a few tens of atomic layers. A molecular electronic device may have several carbonaceous layers such as polymers and e-beam deposited layers that have nearly identical chemical composition and nearly no difference in their mean atomic number and their mean inner potential (MIP).

To visualize the layers of such devices in 3D, it is necessary to use an imaging method that provides sufficient contrast between the materials the device is composed of. Often the contrast of bright field transmission electron microscopy (BFTEM) or annular dark field scanning transmission electron microscopy (ADF STEM) is too low and would require high irradiation dose to obtain adequate signal to noise ratio (SNR) for reliable 3D reconstruction (Hayashida and Malac, 2016). The high irradiation dose implies extensive radiation damage (Egerton et al., 2004) and unreliable reconstructed volume. High angle annular dark field (HAADF) in scanning TEM (STEM) can distinguish device layers that have large differences in their mean atomic number, but does not sufficiently differentiate between low mean atomic number layers, such as Si from silicon oxides or carbon films deposited by electron beam evaporation (e-carbon) from polymers. Elemental mapping using core loss electron energy loss spectroscopy (EELS) requires high irradiation dose due to small inelastic cross section leading to long acquisition time and extensive sample damage. The use of plasmon excitations is not desirable due to high delocalization of the signal (Wang et al., 2008).

While the use of spherical aberration (C_S) correctors can decrease the acquisition time by increasing beam current, it does not reduce the radiation damage of the sample (Egerton et al., 2004). The use of spherical aberration corrector implies high convergence angle of the incident beam in STEM and consequent geometrical beam broadening in the sample (Hayashida and Malac, 2016). The high convergence angle is not desirable for 3D reconstruction of practical samples because it reduces the sample volume that can be examined (Hayashida and Malac, 2016). Typically, to observe the entire device structure, such as a transistor in 3D, a cube of data $\sim 100 \times 100 \times 300\,\text{nm}^3$ of data needs to be examined. Isotropic ~ 1 nm resolution in the reconstructed volume can be obtained for this size of sample when a small convergence of the incident beam in STEM is utilized to avoid geometrical beam broadening in the sample (Hayashida and Malac, 2016). While ADF STEM works well when imaging samples with large difference in their

* Corresponding author.
E-mail address: misa.hayashida@nrc-cnrc.gc.ca (M. Hayashida).
[1] Current address: Applied Materials, Inc., 330 Scott Blvd, Santa Clara 950 USA.

https://doi.org/10.1016/j.micron.2018.09.005
Received 31 July 2018; Received in revised form 6 September 2018; Accepted 7 September 2018
Available online 07 September 2018
0968-4328/ © 2018 Published by Elsevier Ltd.

mean atomic number (Hayashida et al., 2015), it does not help with low mean atomic number sample with a small difference in MIP.

It is possible to obtain phase contrast from low mean atomic number layers with small difference in MIP using a HFPP (Danev et al., 2014; Fukuda et al., 2015; Hettler et al., 2018; Malac et al., 2017, 2012, 2010). HFPP utilizes a uniform thin film placed in the back focal plane of the objective lens, to achieve a phase shift between the direct and diffracted beams (Malac et al., 2010, 2012). The HFPP does not suffer from image contrast ringing due to the cut-on spatial frequency as seen in Zernike phase-plate where direct beam is passed through a hole in a film or in a device (Malac et al., 2012). Recently, a particular implementation of the HFPP concept referred to as a Volta Phase Plate (Danev et al., 2014) has been combined with electron tomography to observe thick biological specimens (Fukuda et al., 2015). The contrast improvement provided by the phase plate was confirmed in projection images of 400 nm thick biological samples.

The applicability of HFPP to thick materials science samples and electron tomography in materials science has not previously been demonstrated. Here we report 3D imaging of a transistor from a smartphone processor chip and a molecular electronic junction using HFPP combined with electron tomography. To ensure isotropic reconstruction of the sample volume, we fabricated a rod-shaped sample of a transistor with 250 nm diameter using a focused ion beam (FIB). Furthermore, we measured interface roughness between e-carbon and bromo-phenyl of the molecular electronics device using a rod-shaped sample with 150 nm diameter. To gain insights in the image contrast origin, we observed a multi-layer test sample composed of carbon/silicon oxide (SiO_x) /silicon nitride (SiN)/ silicon (Si) to quantify the relationship between sample thickness, composition and contrast for each layer with and without HFPP.

We start by describing the experimental procedure. We then present the experimental results for the smart phone processor chip, molecular electronics device and multilayer test sample. Then we discuss results of strong phase object simulations of the multilayer to guide the interpretation of future data.

2. Experimental set up

In this section we discuss the experimental set up used to obtain the data and to reconstruct the 3D volume.

Two rod-shaped samples were prepared by standard micro-sampling method using a dual beam (FIB/SEM) instrument (Hitachi NB-5000). The sample containing the smart phone transistor had ~250 nm diameter while the molecular electronic junction had 150 nm diameter. As shown in Fig. 1a, a custom made sample tip was designed for a JEOL 2200 FS in our laboratory to accommodate a Hitachi needle sample holder (Yaguchi et al., 2008) enabling a full 0° – 180° tilt range of the FIB-fabricated sample rod. The HFPP hardware was installed in the back focal plane of the objective lens of the JEOL 2200 FS TEM / STEM equipped with a cryo-polepiece allowing utilization of the full range of microscope magnification from 500x to 800,000 ×. The HFPP was heated to about 200 °C to avoid extensive contamination (Hettler et al., 2017, 2018; Malac et al., 2012). The objective lens and condenser lens currents were kept constant during the data acquisition to ensure that the cross-over of the back focal plane always coincides with the HFPP plane. The tomographic tilt series was acquired utilizing manual acquisition within the TEMography.com Recorder software package (https://www.temography.com). Sample focusing was achieved by the mechanical z-height control of the sample stage with $\Delta z \approx 1$ nm step. A 3° tilt step over the [-90°, 90°] tilt range was used for both samples. The projected images were 2048 × 2048 pixels with a 0.24 nm pixel size for the transistor and 2048 × 2048 pixels with a 0.144 nm pixel size for the molecular electronics junction. Each tilt series was acquired in about 1.5 h. The projected images were aligned using nano-dots markers in our in-house developed script as described in (Hayashida et al., 2014) correcting for image lateral shift and rotation. After the alignment of the reconstruction was performed using simultaneous iterative reconstruction technique (SIRT) for the transistor and simultaneous algebraic reconstruction technique (SART) for the molecular electronics junction as implemented in the TEMography.com Composer software package (https://www.temography.com).

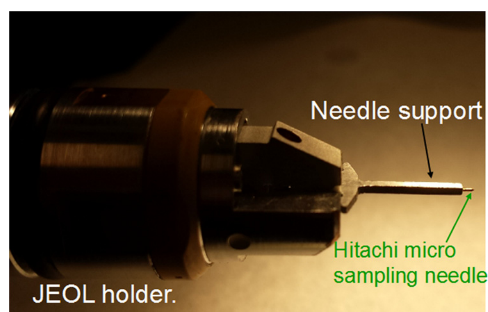

Fig. 1. Arrangement of the sample holder. A standard single tilt JEOL holder with a spring loaded sample rod clamp was used. A needle support with cross sectional dimensions ~1 mm was manufactured to ensure that at ± 90° tilt the needle support does not interfere with pole pieces and cryo box. The sample rod with ~100 to 300 nm diameter was supported on a Hitachi micro sampling needle.

Additionally, we fabricated a multilayer test sample composed of a 20 nm carbon, 40 nm SiO_x and 30 nm thick SiN layers on a silicon substrate to observe the relationship between image intensity and thickness. The layers were perpendicular to the rod long axis. The sample was fabricated on a silicon nitride TEM support window (http://www.norcada.com/products/nitride-windows-tem/) which has a silicon frame covered by a silicon nitride layer. The SiO_x and carbon layers were deposited by electron beam evaporation and ion beam deposition, respectively. Three rod-shaped samples were fabricated with 100, 200 and 300 nm diameters using Hitachi NB 5000 FIB/SEM. Before the rod shaped sample fabrication a 1 μm thick carbon layer was deposited on the surface to protect it from ion beam damage and Ga implantation during ion beam milling. The multilayer samples were used to understand the image contrast observed in the smart phone transistor and molecular electronics samples.

3. HFPP image of a transistor in 3D

The Fig. 2a is a selected projected image from a tilt series of a transistor from a smartphone chip. Fig. 2b shows a contrast reversed reconstructed image of a transistor within a rod with 250 nm diameter from a tilt series (Movie 1) which were taken utilizing HFPP. Fig. 2c and d are z and x slice images of Fig. 2b. Fig. 2e and f are z and x slice images extracted from a reconstructed volume obtained from a BFTEM tilt series (Movie 2) without HFPP. Obviously, the SiO_x contrast between poly Si and Si or poly Si and NiPtSi is clear in Fig. 2c. On the contrary, due to the small difference in the MIP of the Si and SiO_X (Völkl et al., 1999) the BFTEM images in Fig. 2e and f exhibit a low contrast. To sufficiently differentiate the Si and SiO_x layers using BFTEM, a large defocus of the imaging lens would have to be applied, leading to large delocalization of the image contrast.

The contrast of the slice images in Fig. 2c and d has a low pass filtered image appearance, as expected for HFPP images. This is because in HFPP, unlike in a typical BFTEM image, the low spatial frequencies are not absent (Malac et. al 2012). The mottled contrast appearing on the outer surface of the sample rod arises from Ga damage during the sample fabrication using a FIB.

4. Interface of molecular electronic junction visualized in 3D using HFPP tomography

Figs. 3a and b are images of a molecular electronic junction

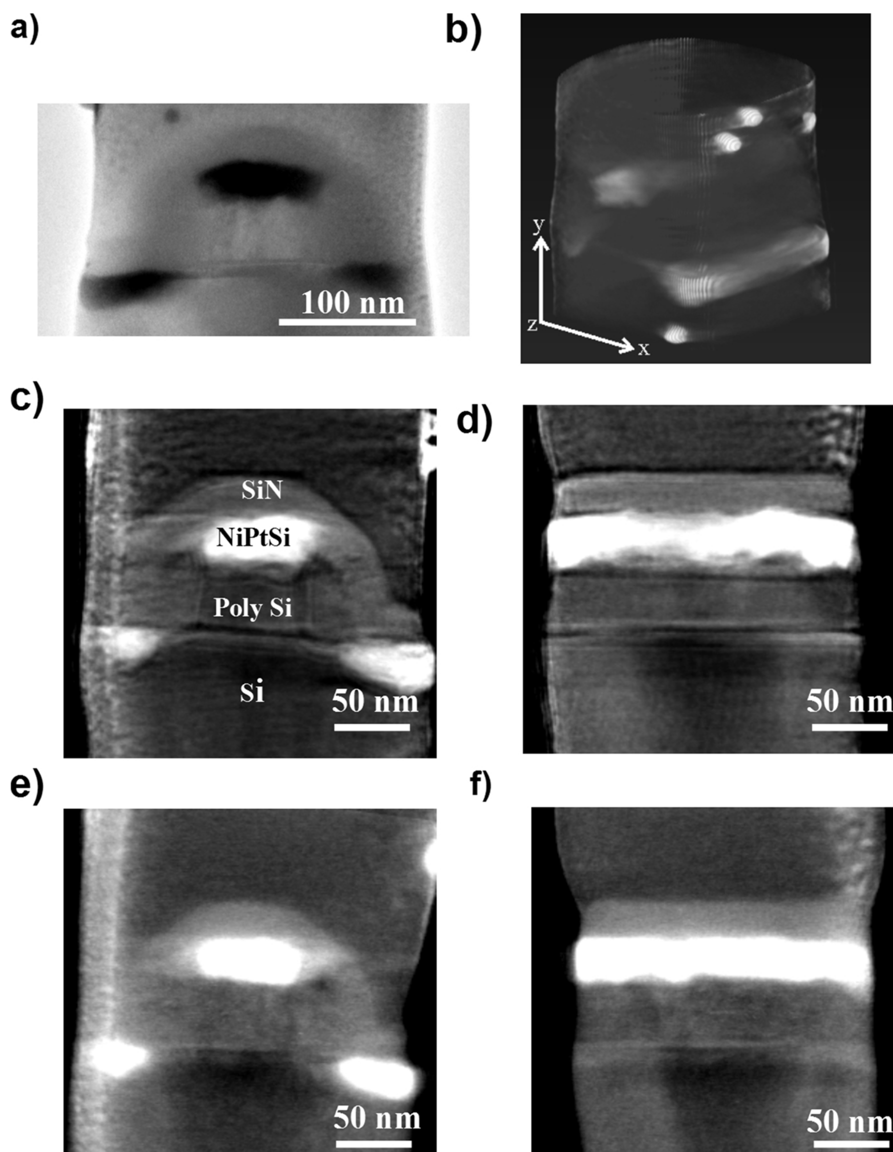

Fig. 2. A smart phone processor chip. a) A selected BFTEM image from tilt series. b) Contrast reversed volume rendering of the 3D volume reconstructed from HFPP images. c) and d) z and x cross sectional slices extracted from the 3D volume from a). The slice in c) and d) are in a plane that is perpendicular one to another. e) and f) z and x cross sectional slices extracted from the 3D volume from a tilt series without HFPP.

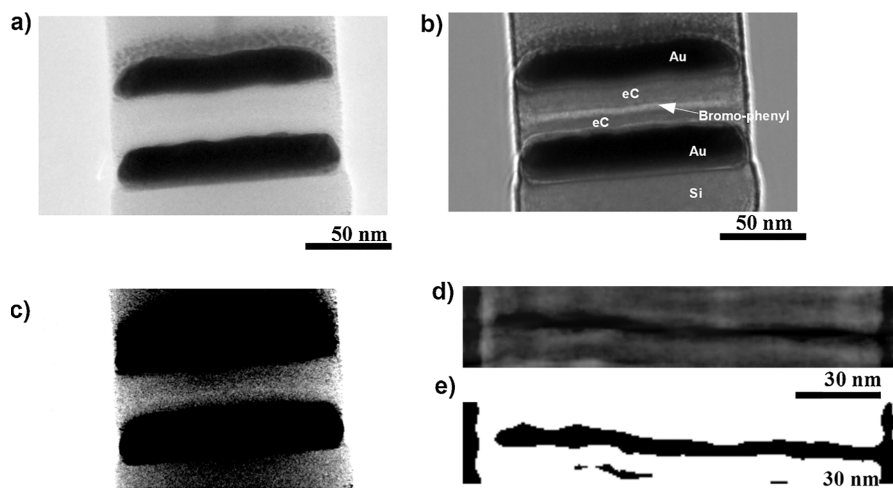

Fig. 3. a) A BFTEM image of molecular electronic junction. b) A HFPP image of the same area as a). c) A contrast enhance image of a). d) A slice extracted from a 3D reconstructed volume obtained from tilt series with HFPP. e) Binary version of d).The image is then used to evaluate interface roughness of the bromo-phenyl layer.

(Morteza Najarian et al., 2016) at in-focus position acquired without and with HFFP respectively. No contrast between electron beam evaporated carbon (eCarbon) and the bromo-phenyl is visible in a BFTEM image without HFPP in Fig. 3a. Even when the contrast is enhanced a lot, difference of the two layers is very small as shown in Fig. 3c. On the contrary, the HFFP image in Fig. 3b provides clear contrast of the same area of the sample.

To retrieve interface roughness (Homeniuk et al., 2018) between the carbon and bromo-phenyl interface, the X–Y cross-sections extracted from the reconstructed 3D volume were processed by applying a median filter with window size 3 pixels as shown in Fig. 3d and converted to binary images (Hayashida et al., 2015) as shown in Fig. 3e. Then, the interface between black (digital 0) and white (digital 1) was detected as interface of the layers. The interface roughness of both top and bottom eCarbon-bromo-phenyl interface was measured (Homeniuk et al., 2018). The RMS roughness of upper interface between eCarbon and Bromo-phenyl is 1.0 nm and 0.85 nm for lower interface between bromo-phenyl and eCarbon. Detail of the results obtained on this sample together with wavelet transformation representation of interface roughness is described in a recent paper (Homeniuk et al., 2018).

5. A multilayer test sample provide insights into contrast dependence on materials properties

To gain insight into the contrast formation in Figs. 2 and 3 we fabricated a test multilayer sample shown in Fig. 4a. Fig. 4b shows images of the test sample with 100 nm, 200 nm and 300 nm diameter with and without HFFP. All images were taken with 2 s exposure time under the same lens condition of the TEM. Fig. 4c shows relationship between contrast and thickness for each layer for the samples obtained in both BFTEM and HFPP imaging mode. The thickness-normalized image contrast used here is:

$$C = (I_{vac} - I_{smpl}) / (t * I_{vac}) \tag{1}$$

here C is contrast for a given material normalized by sample thickness: t, I_{vac} is the intensity (digital counts) in vacuum region of the image and I_{smpl} is the image intensity (digital counts) in center of the sample region of a given composition, e.g. Si, SiN, SiO_2 and Carbon.

Fig. 4c provides insights in the effect of HFPP on image contrast. It shows that the HFPP thickness normalized contrast increases with decreasing rod diameter and with decreasing density. Not surprisingly, the BFTEM thickness normalized contrast in the same figure shows little dependence on rod diameter for the rather small rod diameters examined here (Reimer and Kohl, 2008).

Figs. 2–4 demonstrate that HFPP can be used to obtain contrast from amorphous sample composed of light elements or regions of a sample where the light element low mean atomic number region does not overlap with high mean atomic number region. HFPP also enhances contrast between two materials with similar mean atomic number and similar mean inner potential such as Si, SiN and SiO_2. The origin of the enhancement is discussed in the next section.

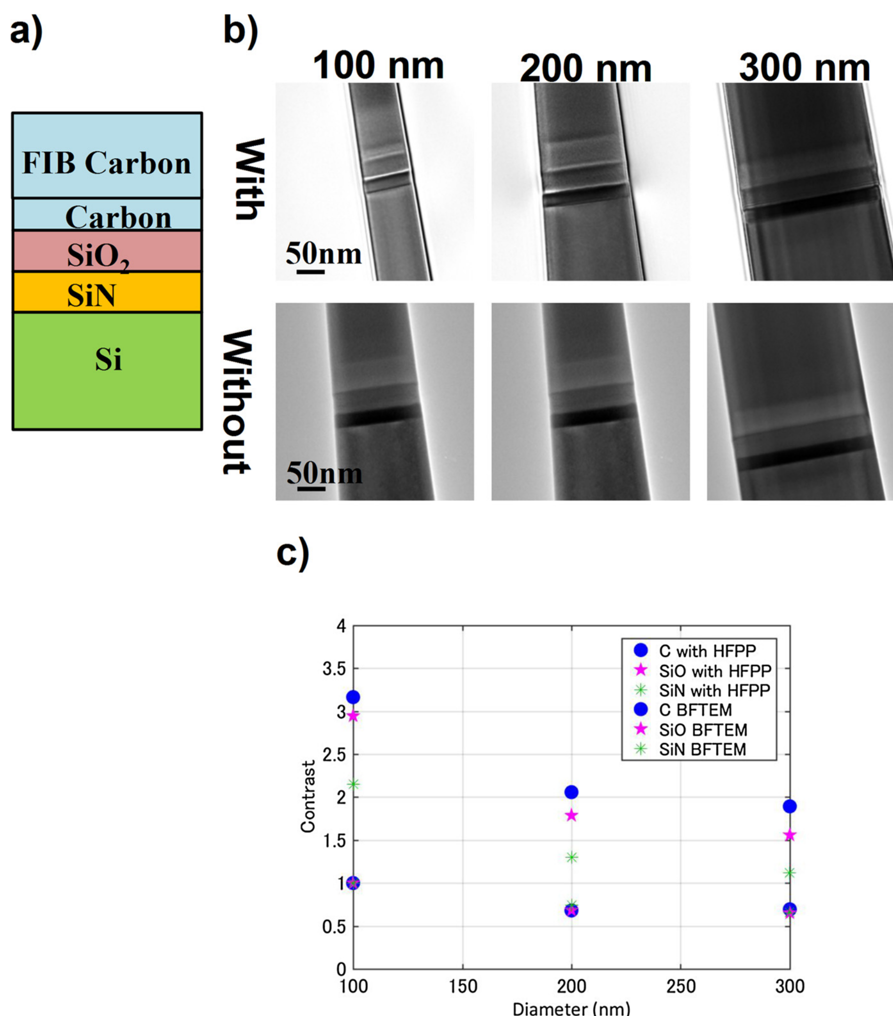

Fig. 4. a) Composition of the test sample.b) BFTEM images of 100, 200 and 300 nm diameter rod-shaped test samples with and without HFPP. c) Contrast observed for C, SiO, SiN for 100 nm, 200 nm and 300 nm rod diameters.

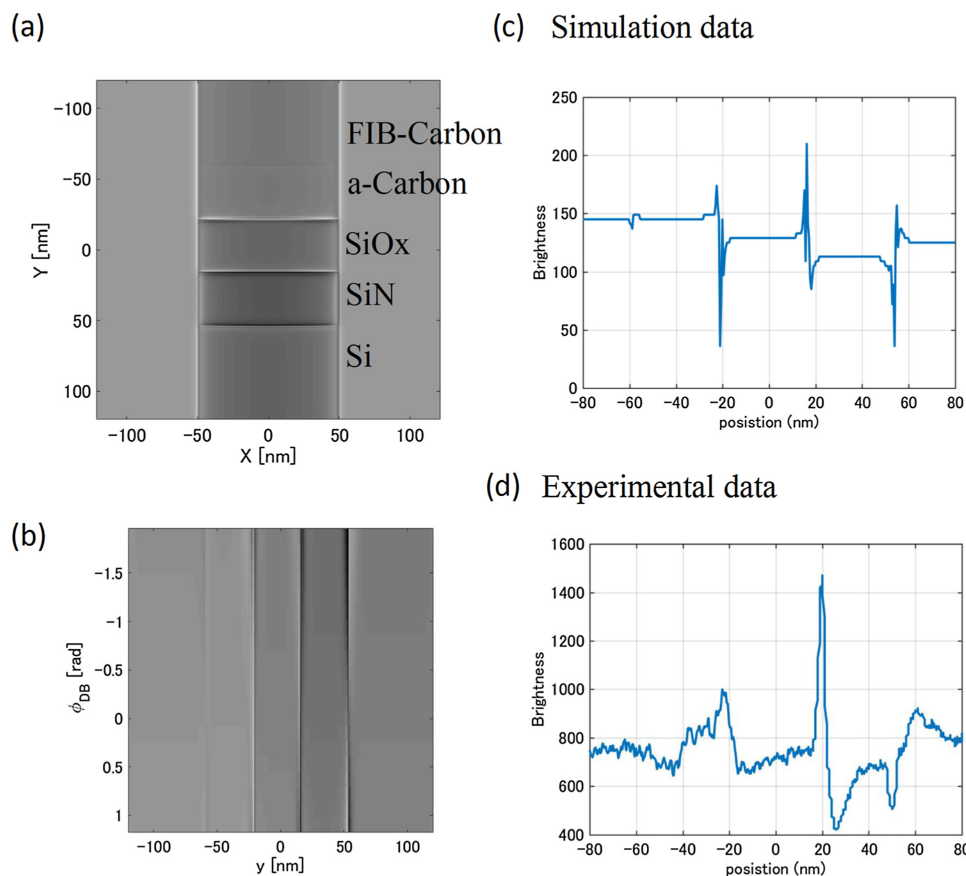

Fig. 5. a) Simulated image of a test sample with 100 nm diameter when phase shift is -0.5 rad. b) Brightness of center of the rod with phase shift for the rod with 100 nm diameter. c) A line profile of brightness of center of the rod. d) A line profile of brightness of center of the rod with 100 nm diameter from Fig. 4b.

6. Computer simulations provide insight into contrast

This section presents computer simulations intended to provide insight into the origin of contrast and reveal potential artefacts. Furthermore, the simulations can be used to understand the limits of HFPP imaging of thick materials science samples. The approach and sign convention described in detail in (Malac et al., 2017) were used for simulations presented here. A Lorentzian-shaped direct beam phase shift $L_1(q)$ of the direct beam relative to the scattered beam (Malac et al., 2012, 2017) was used with magnitude of the direct beam phase φ_{db} = -0.5 rads and width $q_c = 0.025\ nm^{-1}$ at a spatial frequency q as shown in Eq. (2).

$$L_1(q) = \varphi_{db}/(1 + (q/q_c)^2) \quad (2)$$

For the wave aberration function (Eq. (1) in (Malac et al., 2017)), spherical aberration Cs = 2 mm and defocus Dz = 85 nm were used. Incident electron energy was 200 keV in the simulations. An example of simulated image with 100 nm diameter of a test sample which is composed of a 30 nm thick amorphous carbon, 30 nm SiO_x and 30 nm thick SiN layers on a silicon substrate is shown in Fig. 5a. On the amorphous carbon, a hypothetical carbon layer with 0.1 eV higher MIP carbon is placed on the e-beam carbon layer to evaluate contrast arising from materials with very small difference in MIP, such as e-beam and a carbon film deposited by FIB in Fig. 4a. The inner potential of each region is 7.1 V (top section), 7 V (amorphous carbon), 11.2 V (silicon oxide), 15 V (silicon nitride) and 12 V (silicon), respectively (Völkl et al., 1999). The resulting image is darker in the area with sample than in nearby vacuum in agreement with experimental image in Fig. 4b. The contrast of the rod and interfaces depends on phase shift of the HFPP as shown in Fig. 5b which is extracted brightness from center of a rod with 100 nm diameter imaged with a different phase shift $L_1(q)$ stacked along the horizontal axis. For example, the interface between SiO_x and SiN is dark on SiO_x side and bright in SiN side when the $L_1(q)$ phase shift is positive. The reverses when the phase shift is negative. The phase shift was taken φ_{db} = -0.5 rads for simulations shown in Fig. 5a. Fig. 5c and d are line profiles along the center of a rod from an experimental image (Fig. 4b) and a simulated image (Fig. 5a). Although they are not quantitatively matching, the position of peaks and valleys at each interface appears to reproduce the experimental profile qualitatively. The extracted brightness from center of a rod with 200 and 300 nm diameter imaged with a different phase shift is shown in Supplemental Fig. 1a and b.

The asymmetry of the Fresnel-like fringe at the outside of the sample rod seen in Fig. 4a (dark on the right side and bright on the left side) is discussed in this paragraph. There are several possible explanations, such as beam tilt, presence of an off-centre objective aperture, difference in the defocus value on the left and right side of the sample rod if that is far from round cross section profile and a phase shift of HFPP that is not radially symmetric. The simulation of the effect of off center objective aperture (not shown) indicate that the effect of the objective aperture centering is not sufficiently strong to explain the large difference in the appearance of the dark (right side) and bright (left side) fringe on the outside of the sample rod. Similarly, the beam tilt required to explain the difference of the fringes outside of the sample rod is too large and not apparent during the microscope alignment. The difference in the defocus value between the left and right side of the sample rod would have to be larger than the entire sample diameter (100 nm in Fig. 4b). Therefore the possible explanation rests in phase shift of the HFPP that is not symmetric between left and right hand side. To provide insight in the effect of variation in symmetry of the HFPP phase shift on the observed image contrast we modified the phase shift at the HFPP by adding a Lorentzian $L_2(q)$ as shown in Eq. (3)

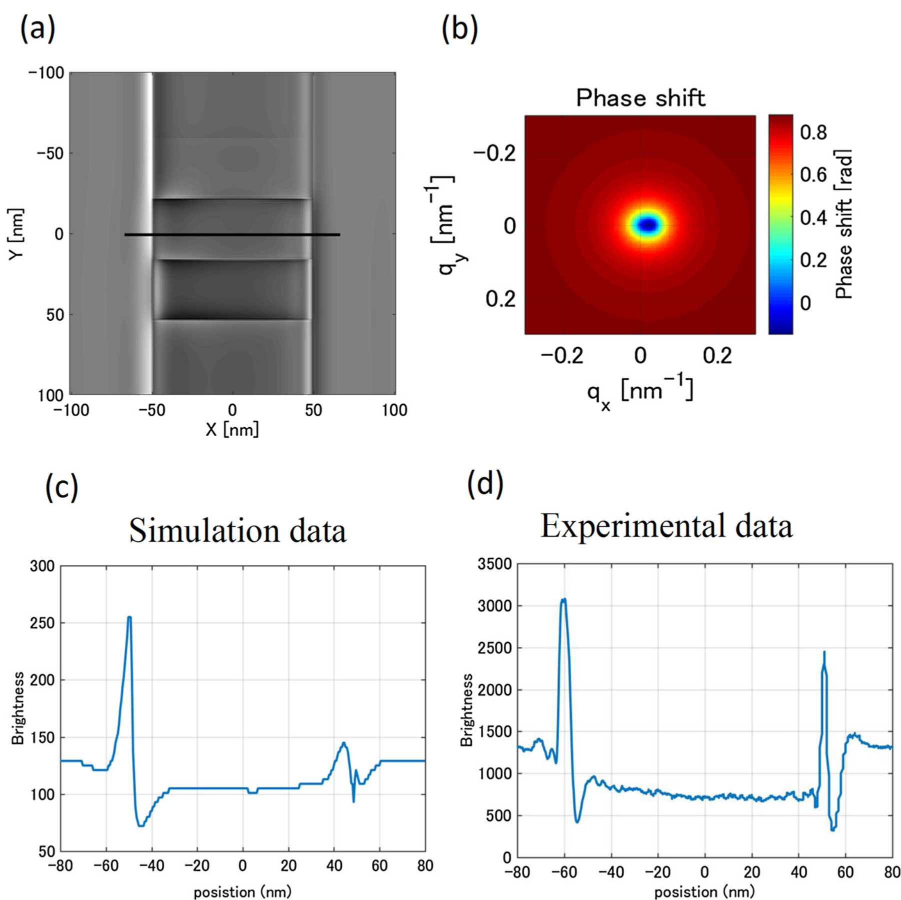

Fig. 6. a) Simulated image of a test sample with 100 nm diameter when phase shift is -0.5 rad and the not symmetric as shown in b). b) Non-symmetric phase shift at $\varphi_{sb} = 1.5\varphi_{db}$, q_s = 3e-2 nm^{-1} and q_c = 0.025 nm^{-1}. c) A line profile of solid line in a). d) A line profile of Vacuum/SiO_2/ Vacuum of the rod with 100 nm diameter from Fig. 4b.

with φ_{sb} as phase shift, q_s as separation of the side beam and width as the direct beam phase shift.

$$L_2(q) = \varphi_{sb}/(1 + ((q + q_s)/q_c)\ \hat{}2) \quad (3)$$

We then simulate the image as function of increasing magnitude of phase shift of the side Lorentzian up to the maximum of 2 phase shift of the direct beam. A 100 nm diameter rod was chosen as it shows not only the side fringes but also reversal of image contrast at the interface between the layers of the sample. An example simulated image for 100 nm sample rod with $\varphi_{sb} = 1.5\varphi_{db}$, q_s = 3e-2 nm^{-1} and q_c = 0.025 nm^{-1} is shown in Fig. 6a. Phase shift with the parameters is shown in Fig. 6b. The components are same as a rod in Fig. 5a. Fig. 6c shows a line profile of a solid line in Fig. 6a and d is a line profile from amorphous carbon region from 100 nm diameter rod in Fig. 4b. Shape of the two line profiles are qualitatively matching. Therefore, the reason for asymmetry of the Fresnel-like fringe at the outside of the sample rod is likely an asymmetry of HFPP of phase shift. The possible origin of the lack of symmetry can include the splitting of the beam due to Bragg reflections in crystalline material, e.g. the silicon portion of the sample rod in Figs. 2–4, forming split beam at the HFPP plane and charging non symmetric area. Alternatively, non-uniformities of the HFPP film itself can perhaps lead to non-uniform HFPP charging. First, the effect of Bragg diffraction splitting is unlikely to be the reason for the beam splitting at the HFPP because for the typical focal length (~2 mm) of an objective lens, 0.2 nm to 0.3 nm lattice spacing and 200 keV incident electron energy, the footprint of the Bragg angle is 12.5 mrad and 8 mrad respectively and the beam is 25 um and 16 um from the central beam, much too far to be of concern even if the Bragg beam intensity was high (as could be the case for a few hundred nm diameter Si rod close to a strongly diffracting condition). As a matter of fact, the footprint size is typically a few tens of nm (Hettler et al., 2017, 2018) with the full width at half maximum of the phase shift Lorentzian in the order of 100 nm–200 nm (Malac et al., 2012). The distance of the direct beam and side beam Lorentzians L_1 and L_2 was $q_s = 3 \times 10^{-2}$ nm^{-1} (75 urad) corresponding to 150 nm between L_1 and L_2 at HFPP when the focal length is 2 mm. The spatial dimensions of the object that could lead to splitting of diffracted beams at the above distance is about 33 nm. At the 3×10^{-2} nm^{-1} the magnitude of the Fourier transform of the object (100 nm diameter rod) is much too low to account for the lack of radial symmetry. We therefore suggest that the origin of the non-symmetric fringes is the non-uniformity of the HFPP film that would produce an elliptical charged patch on the HFPP with the direct beam placed off center on the HFPP (Malac et al., 2012). The possibility of HFPP non being on plane leading to Bragg reflection being at a distance close to 150 nm can be excluded as the off plane position of HFPP can be clearly observed by out of focus Ronchigram contrast arising from the HFPP present in the image. Simulated images for 200 nm and 300 nm rods with the same parameters are shown in Supplemental Fig. 2.

A simulated TEM image of e Carbon/ bromo-phenyl/ Carbon layers taken with HFPP was generated in Fig. 7a that can be compared to experimental data in Fig. 3b. The contrast enhanced BF TEM image without HFPP as shown in Fig. 3c, bromo-phenyl layer is slightly brighter than e Carbon layer. It means that bromo-phenyl layer has lower MIP than e Carbon layer. Therefore, 6.9 V and 7 V are used as MIP for bromo-phenyl and e Carbon for simulation. The intensity profile at the center of the sample rod with different phase shift was shown in Fig. 7b. As mentioned above, phase shift $\varphi_{db} = -0.5$ rad was selected and the position is shown by a dotted line in Fig. 7b. In this case, bromo-phenyl layer is brighter than the Carbon layer and the contrast agrees with experimental data as shown in Fig. 3b. Our previous paper (Hettler et al., 2017) mentioned that the HFPP showed negative phase shift when it was heated at 200°. Our results are therefore additional experimental proof of the HFPP charge polarity.

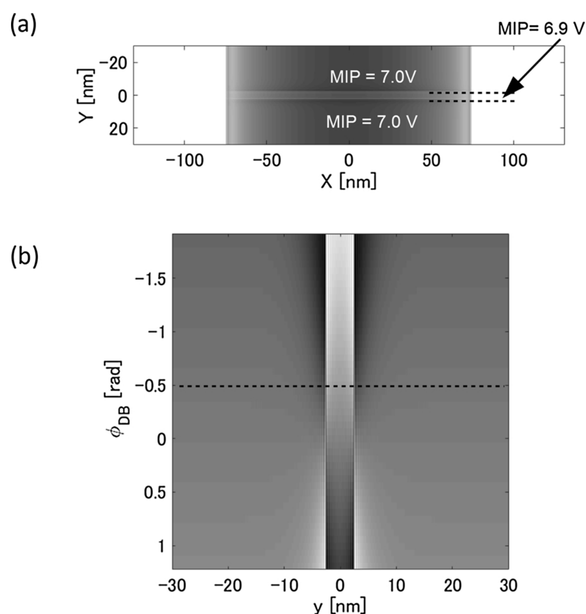

Fig. 7. a) A simulated TEM image of bromo-phenyl/e Carbon/ bromo-phenyl layers taken with HFPP when phase shift is −0.5 rad. b) Brightness of center of the rod with phase shift.

The interface between of bromo-phenyl and e-Carbon shown in Fig. 3b do not have strong fringe between SiN and SiO_x as seen for example in Fig. 5b. This is important fact for electron tomography which requires that the projected image intensities vary monotonically with material thickness to reconstruct proper 3D images. When a material has low mean atomic number and difference of MIP between two different layers, we can avoid the Fresnel-like fringe at the interfaces between the layers which causes artifact in reconstructed images and the contrast is suitable for electron tomography. Therefore, HFPP is useful to observe the detailed 3D structure of materials with low mean atomic number, even in non-biological specimens.

7. Conclusions

We demonstrate that HFPP imaging can be used to obtain 3D visualization of thick materials science samples, although caution is needed to avoid artefacts the HFPP provides suitable projected images for 3D tomographic reconstruction. From experiments and simulation, we found that the contrast depends on the projected phase shift difference within the sample, and that the advantage of the HFPP over BFTEM increases as the sample gets thinner. Moreover, we found that the effect of fringe asymmetry of at interfaces within the sample, in particular between the sample rod and surrounding vacuum, arises from the no symmetric phase shift at the HFPP.

A phase contrast BFTEM often appears as a high pass filtered image, an effect that can lead to inaccurate reconstructed volume (Reimer and Kohl, 2008), whereas HFPP images transfer low spatial frequencies, resulting in low-pass like appearance when compared to standard BFTEM images. The 3D reconstruction by electron tomography leads to loss of high spatial frequencies due to low sampling of the reciprocal space (Hayashida and Malac, 2016) making the HFPP images more suitable for tomography at modest (~1 nm) spatial resolution than BFTEM images that contain high spatial frequencies, only to be lost during the tomographic reconstruction process. However, caution should be exercised to ensure that the HFPP images satisfy the projection theorem (i.e. the contrast is monotonic with sample mass thickness). An indication that the images do not satisfy the projection theorem would be presence of contrast reversals with monotonically increasing sample thickness, e.g. parallel to the sample rod axis.

Acknowledgments

We gratefully acknowledge the support of JEOL Ltd., in particular the support and exciting discussions with Dr. Y. Okura, Dr. Ishikawa and Dr. I. Iijima. The calibration samples used in Fig. 4 were fabricated by Mike O'Toole, NRC-NANO. Prof. Marco Beleggia, Denmark Technical University, helped us to develop the simulations in Malac et al. (2017) that were utilized to simulate the images and movies in this paper.

Appendix A. Supplementary data

Supplementary material related to this article can be found, in the online version, at doi:https://doi.org/10.1016/j.micron.2018.09.005.

References

Danev, R., Buijsse, B., Khoshouei, M., Plitzko, J.M., Baumeister, W., 2014. Volta potential phase plate for in-focus phase contrast transmission electron microscopy. Proc. Natl. Acad. Sci. U. S. A. 111, 15635–15640.
Egerton, R.F., Li, P., Malac, M., 2004. Radiation damage in the TEM and SEM. Micron 35, 399–409.
Fukuda, Y., Laugks, U., Lucic, V., Baumeister, W., Danev, R., 2015. Electron cryotomography of vitrified cells with a Volta phase plate. J. Struct. Biol. 190, 143–154.
Hayashida, M., Malac, M., 2016. Practical electron tomography guide: recent progress and future opportunities. Micron 91, 49–74.
Hayashida, M., Malac, M., Bergen, M., Li, P., 2014. Nano-dot markers for electron tomography formed by electron beam-induced deposition: nanoparticle agglomerates application. Ultramicroscopy 144, 50–57.
Hayashida, M., Ogawa, S., Malac, M., 2015. Tomographic measurement of buried interface roughness. J. Vac. Sci. Technol. B Nanotechnol. Microelectron. Mater. Process. Meas. Phenom. 33.
Hettler, S., Dries, M., Hermann, P., Obermair, M., Gerthsen, D., Malac, M., 2017. Carbon contamination in scanning transmission electron microscopy and its impact on phase-plate applications. Micron 96, 38–47.
Hettler, S., Kano, E., Dries, M., Gerthsen, D., Pfaffmann, L., Bruns, M., Beleggia, M., Malac, M., 2018. Charging of carbon thin films in scanning and phase-plate transmission electron microscopy. Ultramicroscopy 184, 252–266.
Homeniuk, D., Malac, M., Hayashida, M., 2018. Wavelet transform description of buried interface roughness measured by Electron tomography. Ultramicroscopy 194, 64–77.
Malac, M., Kawasaki, M., Beleggia, M., Li, P., Egerton, R.F., 2010. Convenient contrast enhancement by hole-free phase plate in a TEM. Microsc. Microanal. 16, 526–527.
Malac, M., Beleggia, M., Kawasaki, M., Li, P., Egerton, R.F., 2012. Convenient contrast enhancement by a hole-free phase plate. Ultramicroscopy 118, 77–89.
Malac, M., Hettler, S., Hayashida, M., Kawasaki, M., Konyuba, Y., Okura, Y., Iijima, H., Ishikawa, I., Beleggia, M., 2017. Computer simulations analysis for determining the polarity of charge generated by high energy electron irradiation of a thin film. Micron 100, 10–22.
Morteza Najarian, A., Szeto, B., Tefashe, U.M., McCreery, R.L., 2016. Robust all-carbon molecular junctions on flexible or semi-transparent substrates using "Process-Friendly" fabrication. ACS Nano 10, 8918–8928.
Reimer, L., Kohl, H., 2008. Transmission Electron Microscopy. Springer-Verlag, New York.
Völkl, E., Allard, L.F., Joy, D.C., 1999. Introduction to Electron Holography. Springer, US.
Wang, F., Egerton, R.F., Malac, M., McLeod, R.A., Moreno, M.S., 2008. The spatial resolution of electron energy loss and x-ray absorption fine structure. J. Appl. Phys. 104.
Yaguchi, T., Konno, M., Kamino, T., Watanabe, M., 2008. Observation of three-dimensional elemental distributions of a Si device using a 360 degrees -tilt FIB and the cold field-emission STEM system. Ultramicroscopy 108, 1603–1615.